



2.3-cycle mid-infrared pulses from hybrid thin-plate post-compression at 7 W average power

Mate Kurucz^{a,*}, Roland Flender^a, Ludovit Haizer^a, Roland S. Nagymihaly^a, Wosik Cho^{b,c}, Kyung T. Kim^{b,c}, Szabolcs Toth^a, Eric Cormier^{d,e}, Balint Kiss^a

^a ELI-ALPS Research Institute, Dugonics tér 13, 6720 Szeged, Hungary

^b Center for Relativistic Laser Science, Institute for Basic Science, 61005, Gwangju, Republic of Korea

^c Department of Physics and Photon Science, Gwangju Institute of Science and Technology, 61005, Gwangju, Republic of Korea

^d Laboratoire Photonique, Numérique et Nanoscience, Université Bordeaux-IOGS-CNRS (UMR 5298), rue F. Mitterrand, 33400, Talence, France

^e Institut Universitaire de France, 1 rue Descartes, 75231 Paris, France

ARTICLE INFO

Keywords:

High-power
Mid-infrared
Post-compression
Thin plate compression

ABSTRACT

Output pulses of a 100 kHz mid-infrared OPCPA system are post-compressed from 4.7 cycles down to 2.3 cycles by using a combination of a dielectric and a semiconductor crystal in a hybrid thin plate setup. Efficient spectral broadening is demonstrated with 11 W average input power. After compression the output power reached 6.8 W with exceptional CEP and energy stability for several hours. The post-compressed pulses were carefully characterized in both temporal and spatial domains, resulting in 2.3-cycle temporal duration at 3.1 μm central wavelength with a temporal Strehl ratio of 0.73 and a spatial Strehl ratio of 0.97. Thermal limitations due to multiphoton absorption of semiconductors present at this power level are explored by temperature measurements, which are supported by detailed numerical simulations. Upscaling for higher average powers was also investigated.

1. Introduction

High repetition rate mid-infrared (MIR) (3–8 μm) laser systems are now being developed at a very high pace due to their applicability to strong-field physics in solid-state media [1], to time-resolved spectroscopy [2], and also to extend the photon cut-off energy in high harmonic generation [3]. Some of these applications require few-cycle carrier-envelope phase (CEP) stable MIR pulses, often achieved by the optical parametric chirped pulse amplification (OPCPA) technique providing large bandwidth and/or spectral tunability. Producing pulses with less than 4 optical cycles in the 3 to 4 μm spectral range remains very challenging based solely on the current OPCPA technology [4–8]. Shorter pulses can be generated by additional compression techniques mainly based on nonlinear spectral broadening [8–19]. In this spectral range, the post-compression of low average power sources has been demonstrated by using noble-gas filled hollow-core waveguides [9,10]. These fibers exhibit around 50% total transmission mainly due to capillary losses and material absorption, which means net peak power is only increased for relatively long initial pulses (>50 fs). This limitation is somewhat mitigated in antiresonant-guiding photonic crystal fibers (ARR-PCFs) [8,11], where transmission around 85% can be achieved.

Multipass cells (Herriott cell) using bulk media [12,13] and recently noble gases [14,15] are promising candidates for post-compression for

wide range of pulse parameters, but to the best of our knowledge, no implementation was presented for MIR wavelengths so far. The reason behind is mainly the scarcity of adequate chirped and broadband HR mirror coatings for the given wavelength range.

A cheaper and much simpler post-compression scheme for intense MIR pulses employs bulk solid-state media [16–19], where the nonlinear refractive index (n_2) is orders of magnitude higher compared to inert gases inside the hollow-core waveguides. With carefully chosen bulk geometry, material choice and divergence control, spectral broadening can be achieved with input pulse energies orders of magnitude above the critical self-focusing limit [17].

Efficient spectral broadening from a single bulk plate is limited by plasma formation due to ionization, which results in nonlinear losses and degradation of the beam profile at higher input intensities [18]. To overcome the limitations of single-plate compression of MIR pulses, different material thin plates of opposite group velocity dispersion (GVD) could be employed in alternating order, in a hybrid setup. Having the appropriate parameters for these plates, such as n_2 , GVD and thickness, may allow to compensate the spectral phase (up to the second order phase) on the subsequent plate, resulting in sufficient intensity to drive the nonlinear broadening efficiently.

In the 3–4 μm wavelength region narrow bandgap semiconductors – unlike dielectrics and most glasses – have positive GVD, which makes

* Corresponding author.

E-mail address: Mate.Kurucz@eli-alps.hu (M. Kurucz).

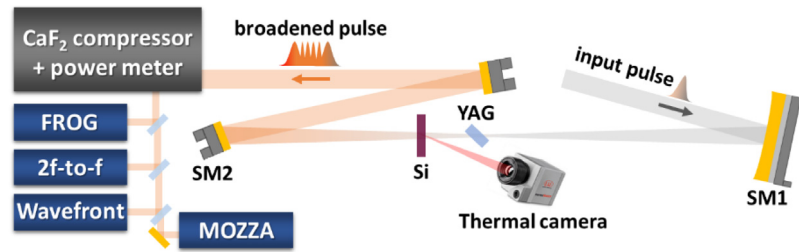


Fig. 1. Schematic view of the experimental arrangement. SM1 and SM2 are concave spherical mirrors.

them an essential component in a hybrid setup. The semiconductors have higher linear and nonlinear losses compared to dielectrics, based on band model calculations and previous measurements [18,20]. This can lead to serious local temperature increase with high average power driver lasers. At the level of multiple tens of watts, limitations may occur such as thermal lensing, stress induced damage, and even disturbances of ambient air around the semiconductor plate caused by the heat exchange.

In this paper, we demonstrate the highest average power semiconductor-dielectric hybrid thin plate post-compression, achieving 2.3 optical cycles from the initial 4.7 cycle pulses, centered at $3.1 \mu\text{m}$. The significant temperature rise of the semiconductor thin plate was monitored during the experiment, which provided useful input data for numerical simulations. Further upscaling in terms of average power was investigated, based on the results of numerical simulations.

2. Experimental technique

Extension capabilities of the MIR laser system of ELI-ALPS [5,21] emitting at $3.2 \mu\text{m}$ central wavelength were investigated by using a post-compression scheme based on nonlinear broadening in centrosymmetric crystals. Several aspects were considered to find the optimal crystals for the task: nonlinear refractive index, spectral transmission, GVD, bandgap and multiphoton absorption parameters. Note that all materials have positive specific third order dispersion, which can limit pulse compressibility. In order to decouple the spatial and spectral impact of the Kerr effect and to gain precise control of material dispersion the application of millimeter thin nonlinear media is required.

Furthermore, as the MIR laser system provides relatively high average power ($>10 \text{ W}$), the spot size on the material is also limited, since high average power density may easily lead to optical damage through thermal shock in the material. These geometrical constraints prompted us to choose the highest nonlinear refractive index materials to ensure sufficient broadening. Furthermore, nonlinear media with the least amount of linear and non-linear absorption around $3.2 \mu\text{m}$ were preferred.

There are two types of crystal materials that are transmitting in the MIR spectral region: semiconductors with narrow bandgap and dielectrics with wide bandgap. Semiconductors, as it was mentioned in the introduction, have positive GVD at $3.2 \mu\text{m}$ and high nonlinear refractive index ($>10^{-15} \text{ cm}^2/\text{W}$), but because of the narrow bandgap fewer photons are needed for nonlinear absorption, which can decrease transmission at high intensities. On the other hand, dielectrics have negative GVD, but much lower nonlinear refractive index ($<10^{-15} \text{ cm}^2/\text{W}$). Semiconductors as silicon and germanium were the prime candidates as they have the highest nonlinear refractive index of $3.79 \cdot 10^{-14} \text{ cm}^2/\text{W}$ and $3.68 \cdot 10^{-13} \text{ cm}^2/\text{W}$ respectively [22]. Germanium has a bandgap of 0.66 eV, allowing two photon absorption at $3.2 \mu\text{m}$ (0.39 eV). Silicon on the other hand has a bandgap of 1.1 eV, setting the onset of non-linear absorption to three or more photon making it preferable to germanium. Several commercially available dielectrics were also considered: fluorides [23,24], sapphire [24] and YAG [25] out of which YAG has the highest nonlinearity of $7 \cdot 10^{-16} \text{ cm}^2/\text{W}$. These arguments lead us to choose YAG and silicon for the setup, a

combination also proposed by Faming Lu, et al. [18], for a laser with parameters somewhat similar to the ELI-ALPS MIR laser.

The 100 kHz OPCPA system delivered 50 fs compressed pulses (43 fs FTL) at the time of the experiment. An average power of 11 W from the laser was coupled into a focusing arrangement with a $f = 500 \text{ mm}$ focal length gold coated concave spherical mirror (Fig. 1, SM1). First, spectral broadening of the initially 50 fs pulses is examined in individual pieces of uncoated 2 mm thick YAG crystal at Brewster-angle [16], and an AR coated 1 mm thick Si alone, then the combination of these were tested. The thickness of the plates was chosen to optimize both spectral broadening and recompression. Thinner plates have lower B-integral and consequently less SPM at the same input intensities, making them less desirable in this application. Choosing thicker than 1–2 mm Si and YAG has disadvantages with the given input laser parameters. Both material is highly dispersive in this spectral region, meaning that the useful thickness in terms of SPM is limited, as the laser intensity within the plates drops after few millimeter of propagation. Additionally, increasing the thickness of plates, the added positive TOD limits the efficiency of final recompression achieved by bulk materials exclusively. Finally, recompression is performed in a window made of CaF_2 having negative GVD.

A multi-octave spectrum analyzer (Mozza, Fastlite) was used to measure the spectrum of the post-compressed pulses. The average power measurement was performed with a thermopile power meter (UP55M-500W-H12-D0, Gentec-EO). The pulse duration before and after the plates were measured with an SH-FROG device (see detailed description at Chapter 3.2). The beam profile was characterized before and after the focus point with a pyroelectric scanning slit beam profiler (Nanoscan, Ophir). The laser peak intensities on the plates were calculated using these measurements. Fine dispersion tuning is performed via a 100 kHz acousto-optic programmable dispersive filter (Dazzler, Fastlite) in the OPCPA system.

3. Results

3.1. Spectral broadening

Our aim was to achieve sub-20 fs FTL spectral broadening and recompress the pulses close to 2-cycle FWHM pulse duration, while keeping the nonlinear absorption losses as low as possible. In this work, both plates were kept behind the focal plane, measured to be at 505 mm from to the focusing mirror. By increasing the intensity on the plates (achieved by decreasing the distance from the focal plane), losses fairly increase as nonlinear absorption processes inside the silicon and YAG become significant. Moving the YAG at a distance shorter than 525 mm from to the focusing mirror, visible filamentation and self-focusing was observed together with increasing optical losses (similarly as in ref [19] for CaF_2) and spectral instability, then finally optical damage of the output surface. Increasing the intensity on the Si plate gradually increased the nonlinear absorption, which turned into heat, and finally optical damage of the AR coating was observed for peak intensities greater than $300 \text{ GW}/\text{cm}^2$.

The empirically found optimal experimental parameters and results of spectral broadening are quantified in Table 1, and the measured

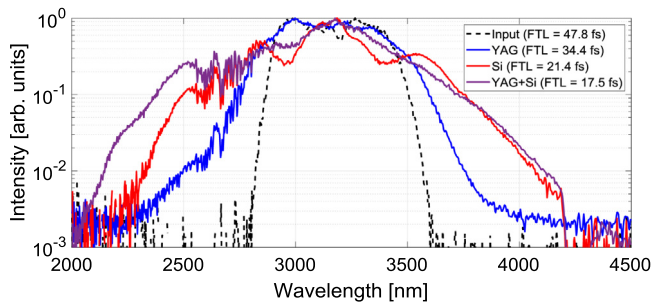


Fig. 2. Measured spectra with different nonlinear media: input reference spectrum (black), with only YAG (blue) at 525 mm, only Si (red) at 580 mm and with YAG (at 525 mm) and Si (at 675 mm) crystals together (purple). (For interpretation of the references to color in this figure legend, the reader is referred to the web version of this article.)

Table 1

Measured parameters of thin-plate compression setup. The FTL duration was calculated from the measured spectra. The values in brackets refer to the distance of the given plate from the focusing mirror.

Material (position)	Peak intensity [GW/cm ²]	Absorption loss [%]	Output energy [μJ]	FTL [fs]
YAG (525 mm)	275	2	104	34.4
Si (580 mm)	207	14	92	21.4
YAG (525 mm) & Si (675 mm)	275 & 77	11	92	17.5

spectra are displayed in Fig. 2. The obtainable FTL duration did not decreased significantly below values shown in Table 1 even at the positions, where intensity (and consequently nonlinear losses) were higher. Output energy refers to pulse energy measured right after the plate(s). The measured reflection losses were around 1% and 2.5% for YAG and Si, respectively. The results show that by using a single plate alone, further spectral broadening beyond 2–3 cycle FTL bandwidth becomes impractical, due to excessive losses.

Finally, the combination of the two crystals was tested. The YAG crystal was placed at its optimal position at 525 mm from the focusing mirror (Table 1). After the YAG the pulses are spectrally broadened and self-compressed [17], which is proved by the measured pulse duration of 36.8 fs with an error of 0.71% RMS. The ideal position for the AR coated Si plate was found to be at 675 mm from the focusing mirror again determined by significant spectral broadening together with reasonably low (~10%) losses due to nonlinear absorption, without any observable optical damage. The calculated B-integral was 0.7 and 3.96 radian inside the YAG and the Silicon plates respectively. This configuration provides 9.2 W with 17.5 fs FTL duration which translates to 1.7 optical cycles at 3.1 μm central wavelength (Fig. 2). The spectral hole at 4.2–4.3 μm is due to CO₂ absorption in air, while the modulation at 2.6–2.7 μm is caused by absorption of water vapor in the air of the laboratory (40% relative humidity).

After propagation through the 2 plates, the beam profile exhibits a sinc intensity distribution due to the spatial Kerr effect. The second spherical mirror (Fig. 1, SM2) collimated the spectrally broadened beam to 8 mm diameter (at 1/e² intensity level). This mirror was specifically chosen to reflect only the central part of the diffraction pattern eliminating the outer rings, which were blocked behind the mirror. This way, only the central part of the intensity distribution was kept, which resulted in an additional loss. All together the beam clipping and the propagation through the various optics resulted in a net loss of 2 W. Finally, the remaining beam (7.2 W) was sent to the bulk compressor, and then to the diagnostics. Due to Fresnel losses, the output average power after the uncoated CaF₂ compressor was 6.8 W (68 μJ).

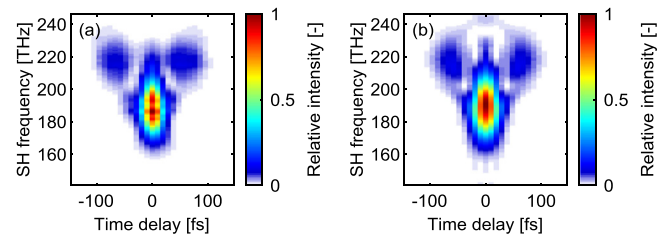


Fig. 3. (a) Measured SH-FROG trace of the post-compressed pulse (with 3.3 mm CaF₂) and (b) reconstructed SH-FROG trace with an error of 1.06% RMS, yielding 22.8 fs FWHM pulse duration.

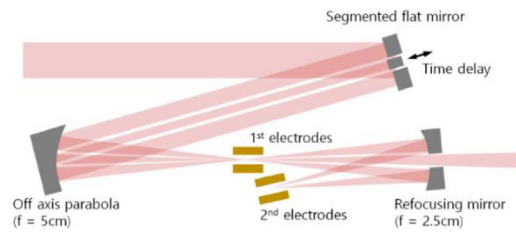


Fig. 4. Schematic representation of all-reflective TIPTOE setup. The modulation of the total ionization yield is recorded as the function of time delay, from which temporal characterization of the post-compressed pulses can be achieved.

3.2. Temporal characterization

Temporal characterization of the compressed pulses was first performed by a home-built all-reflective second-harmonic (SH) based FROG device equipped with an InGaAs based spectrometer (NIR-QUEST512-2.5, Ocean Optics). A 100 μm thick AGS crystal ($\theta = 36.6^\circ$) is used for the SH-FROG, with a spectral acceptance bandwidth of 4100 cm⁻¹ (i.e. from 1.9 μm to 8 μm) at 3.1 μm, which is sufficient to measure the pulses discussed here. Recompression was tested with the available 2, 3.3, 4 and 5 mm of CaF₂ windows, from which the 3.3 mm thick one provided the cleanest temporal profile with an FWHM duration of 22.8 fs (2.3 cycles at 3.1 μm). The measured and the reconstructed SH-FROG traces are shown in Fig. 3 (a–b).

An alternative temporal characterization measurement was also performed with the TIPTOE (tunneling ionization with a perturbation for the time-domain observation of an electric field) method [26]. As detailed in reference [27] the input beam is divided into two parts by a segmented piezo-controlled flat mirror in order to control the relative delay between the outer and inner beam segments, displayed on Fig. 4.

The delayed pulses are recombined and focused into the gap of the first pair of metal electrodes using an off axis parabola ($f = 5$ cm), and the resulting ionization yield is measured as a function of time delay. A holey focusing mirror then refocuses the outer beam on a second pair of electrodes. These electrodes measure the reference (or background) ionization yield, into which the laser fluctuations are imprinted. Finally, the modulation of the ionization yield is calculated as a function of delay, and the reconstruction algorithm computes the electric field and phase of the measured pulses. The measured pulse duration was 23.5 fs (2.3 cycles), which is less than a fs longer than pulse duration retrieved from the FROG measurement. The measured and reconstructed ionization yield is visualized in Fig. 5.

The spectral and temporal intensity distribution of the pulses measured by the two methods are displayed and compared on Fig. 6 (a–d). Based on these results, we have proven that the pulse duration was indeed recompressed to not more than 2.3 optical cycles. On Fig. 6 (c,d) the retrieved spectral phase around 2.6 μm (115 THz) is heavily modulated in both cases, which is a result of the absorption of water vapor due to the humidity content of air. It is also visible in Fig. 3 (a) and (b), where at the higher SH frequencies the FROG traces have a

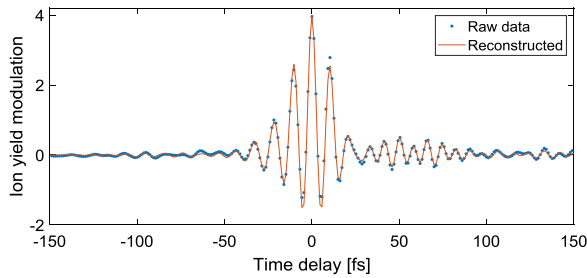


Fig. 5. Raw (blue dots) and reconstructed (red line) ion yield modulation from the TIPTOE measurement, which is not to be confused with the electric field of the laser pulse. (For interpretation of the references to color in this figure legend, the reader is referred to the web version of this article.)

double peak structure at 60 and -60 fs positions. This limits further broadening and compressibility due to the distorted spectral phase. Side peaks can be observed on both reconstructed temporal profiles obtained by the TIPTOE and the SH-FROG techniques Fig. 6 (a,b). TIPTOE confirms that these peaks are post-pulses, as it is sensitive to the direction of time unlike the SH-FROG measurements. Based on the reconstructed spectral and temporal intensity profiles, the temporal Strehl ratio (defined by the ratio of peak powers provided by the measured and that of the transform-limited pulse shape) was calculated to be 0.73, with 90% of pulse energy contained in the main peak.

3.3. Stability and spatial characterization

An eight-hour long stability measurement was performed, where fluctuations of the CEP, output power, and the broadened spectrum were recorded simultaneously. The CEP drift is measured single-shot by a f-to -2f interferometer equipped with a fast fringe detector (Fringeazz, Fastlite) for single-shot CEP measurement, sampled at 10 kHz repetition rate [28]. The measured CEP drift (as error signal) was sent to the Dazzler to correct for fluctuations in a closed-loop mode. The CEP noise was found to be 82 mrad RMS (Fig. 7, a) during the eight-hour measurement, which corresponds to 288 million data points. The CEP has a high frequency noise component, which the stabilization feedback loop was unable to correct, however the majority of the measured data points (>95%) are within the ± 150 mrad interval.

The single-shot long-term energy measurement was performed with a photodetector (PDA10PT-EC, Thorlabs) and tracked with an oscilloscope. The resulting single-shot RMS stability of the pulse energy is 2.4%. An additional power stability measurement was performed with a Gentec-EO power meter, which shows a RMS stability of 0.9% during the same eight-hour period (Fig. 7, b).

The near field spatial intensity distribution (Fig. 8, a) of the compressed pulses was measured by a wavefront sensor (SID4-DWIR, Phasics). The peak-to-valley value of the phase map was found to be 0.3λ , while the RMS was 0.061λ with λ equal to $3.1 \mu\text{m}$. The Strehl ratio (ratio of peak focal intensities in the aberrated and ideal point spread functions) was calculated to be as high as 0.97. The far field distribution was calculated using the measured intensity and phase map of the near field (Fig. 8, b).

3.4. Thermal performance

Due to the relatively high average power of the input beam, thermal effects were expected to rise in the nonlinear media. Therefore, we have monitored the temperature changes in the Si and YAG crystals with a thermal camera (TIM-200, Micro-Epsilon). The temperature distributions are shown in Fig. 9 (a–b). The peak temperature in the Si itself cannot be retrieved correctly due to the overlap between the transmission window of the Si medium and the sensitivity range of the thermal camera of $8 \mu\text{m}$ to $13 \mu\text{m}$, meaning that only the temperature

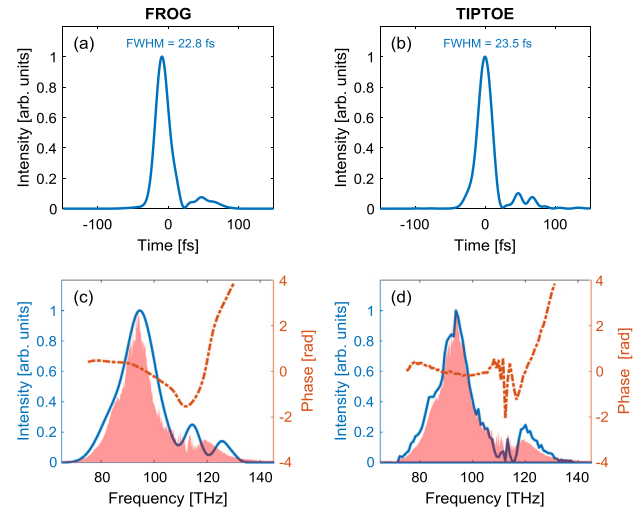


Fig. 6. (a) The reconstructed temporal intensity profile is displayed from the SH-FROG measurement. The FWHM pulse duration is 22.8 fs. (c) The reconstructed spectral intensity (blue line) and phase (orange dashed line) from the SH-FROG trace compared to the Mozza measured spectrum (pink area). (b) The temporal intensity profile reconstructed from TIPTOE yielding 23.5 fs FWHM pulse duration. (d) The spectral intensity (blue line) and phase (orange dashed line) from TIPTOE measurement and the Mozza measured spectrum (pink area). (For interpretation of the references to color in this figure legend, the reader is referred to the web version of this article.)

of the mount itself is representative. To create a 3D thermal model, the measured temperature distribution of the Si mount was used, and the absorbed power was calculated from the multiphoton (3 and 4 photon) absorption process of Si [29].

Temperature rise due to multiphoton absorption in Si was simulated in COMSOL Multiphysics by using the nonlinear absorption coefficients from reference [30]. The geometry of our model consisted of the aluminum mount and the Si crystal. At the outer surfaces a heat flux with a heat transfer coefficient of $5 \text{ W}/(\text{m}^2 \text{ K})$ was taken, which accounted for the passive cooling by the ambient air of the laboratory. In the meantime, cooling through the mount-post assembly was implemented by a heat flux with a heat transfer coefficient of $470 \text{ W}/(\text{m}^2 \text{ K})$ matching the experimental conditions. The absorbed pump power was considered as the heat source in the model, which agreed with the measured power losses after the Si crystal during the experiment. This way, the 3D model was validated with the measured temperature distribution of the mount and the measured absorbed energy.

Based on the validated model, upscaling simulations were conducted for the post-compression of pulses up to 1 mJ input energy at 10 and 100 kHz repetition rates, while keeping the peak intensity in the Si crystal at constant level. Consequently, the rate of the multiphoton absorption was considered to be the same for all energy levels. The temperature elevation in the Si crystal with increasing average power can be seen in Fig. 9 (d). At 100 kHz, even with 200 μJ pulses a peak temperature of 50°C is reached with the same passively-cooled configuration, which was used in the measurement. However, by increasing the pulse energy to 1 mJ at 100 kHz (100 W average power), the temperature is expected to exceed 162°C , which would be undesirable. In comparison, the highest temperature reached with 1 mJ pulses at 10 kHz (10 W average power) is only 35°C . The thermal lens was estimated to be not shorter than 6 m even in case of pulses with 1 mJ at 100 kHz, which is attributed to the high thermal conductivity of Si [31]. Based on these results, active cooling of Si-based post-compression schemes is necessary for pulse energies higher than 200 μJ at 100 kHz, while at 10 kHz no cooling of the nonlinear medium is required up to 1 mJ pulse energy.

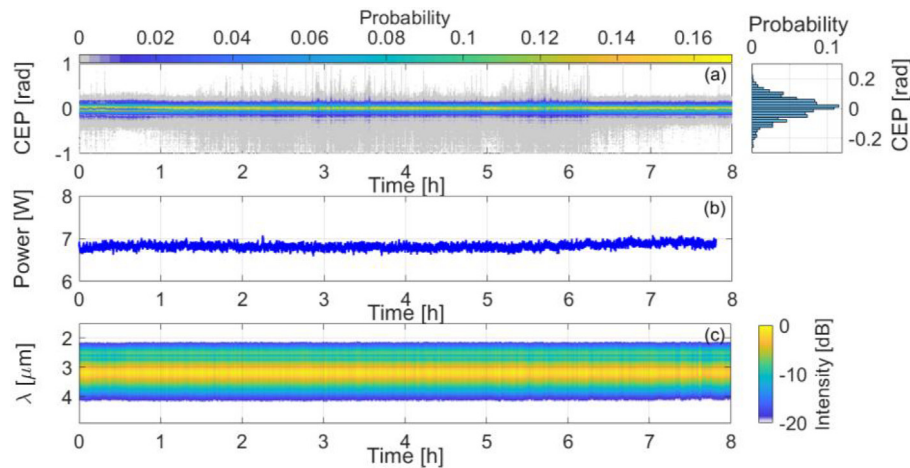


Fig. 7. Eight-hour long stability measurement of post-compressed pulses. (a) CEP stability, (b) power stability and (c) spectral intensity was measured in parallel.

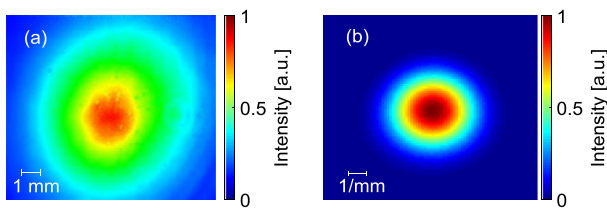


Fig. 8. (a) Near field spatial profile of the post-compressed beam measured with the wavefront sensor. (b) Calculated far field intensity distribution.

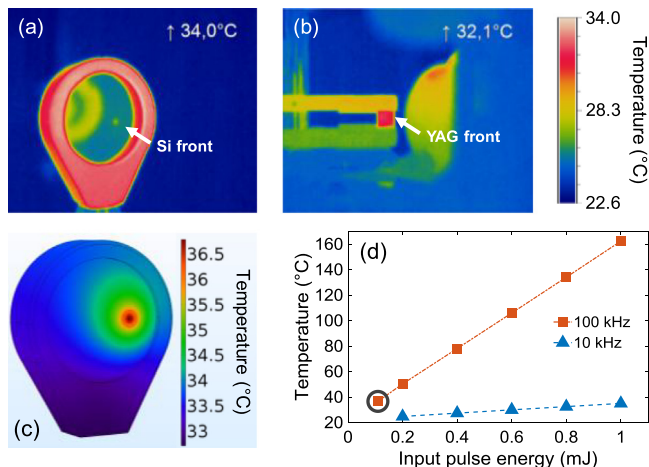


Fig. 9. Thermal camera pictures of in the Si (a) and YAG (b) crystals and in their mounts. Temperature in the upper left corner refers to the maximum temperature of the images. (c) Simulated 3D temperature distribution in Si and its mount. (d) Peak temperature in the Si plate for upscaling in pulse energy for 100 (orange squares) and 10 kHz (blue triangles) repetition rates. Gray circle in (d) denotes the measured data point. (For interpretation of the references to color in this figure legend, the reader is referred to the web version of this article.)

4. Conclusions

In conclusion, we have demonstrated to the best of our knowledge the highest average power semiconductor-dielectric hybrid thin plate post-compression arrangement, demonstrating 23.5 fs pulse duration in MIR spectral region with 6.8 W output. The pulses were characterized in both temporal and spatial domains. The CEP, pulse energy and output spectrum of the laser was monitored for 8 h continuously revealing very good long term stability. Thermal limitations were investigated

in the current optical scheme by merging experimental measurements and thermal simulations. Based on the achieved results, we predict that without active cooling, temperature elevation in the silicon (or other semiconductor plates) will limit the upscaling of the presented post-compression method for higher average powers.

The presented CEP-stable MIR source is attractive for applications in the strong-field science and CEP sensitive time-resolved experiments. Given the parameters, including the Strehl ratio, in the focus of a 2-inch focal length parabolic mirror the local intensity can easily reach values above 10^{14} W/cm². The first user experiment, which required high intensity, sub-3 cycle CEP stable MIR pulses, has been successfully performed and published [32] using the source described in this paper.

Declaration of competing interest

The authors declare that they have no known competing financial interests or personal relationships that could have appeared to influence the work reported in this paper.

CRediT authorship contribution statement

Mate Kurucz: Investigation, Software, Writing - original draft, Visualization. **Roland Flender:** Investigation, Methodology, Validation. **Ludovik Haizer:** Data curation, Investigation. **Roland S. Nagymihaly:** Investigation, Software, Visualization, Writing - review & editing. **Wosik Cho:** Investigation, Software. **Kyung T. Kim:** Investigation, Software. **Szabolcs Toth:** Investigation. **Eric Cormier:** Conceptualization, Writing - review & editing. **Balint Kiss:** Conceptualization, Investigation, Methodology, Project administration, Supervision, Validation, Writing - review & editing.

Acknowledgments

ELI-ALPS (GINOP-2.3.6-15-2015-00001); Nemzeti Tehetség Program (NTP-NFTÖ-18-B-0414); Eric Cormier acknowledges funding from the Institut Universitaire de France. Wosik Cho and Kyung Taek Kim were supported by the Institute for Basic Science (IBS-R012-D1).

References

- [1] B. Wolter, M.G. Pullen, M. Baudisch, M. Sclafani, M. Hemmer, A. Senftleben, C.D. Schröter, J. Ullrich, R. Moshhammer, J. Biegert, Strong-field physics with mid-IR fields, *Phys. Rev. X* 5 (2015) 021034, <http://dx.doi.org/10.1103/PhysRevX.5.021034>.
- [2] Z. Heiner, L. Wang, V. Petrov, M. Mero, Broadband vibrational sum-frequency generation spectrometer at 100 kHz in the 950–1750 cm⁻¹ spectral range utilizing a LiGaS₂ optical parametric amplifier, *Opt. Express* 27 (2019) 15289–15297, <http://dx.doi.org/10.1364/OE.27.015289>.

- [3] T. Popmintchev, M.-C. Chen, D. Popmintchev, P. Arpin, S. Brown, S. Ališauskas, G. Andriukaitis, T. Balčiūnas, O.D. Mücke, A. Pugzlys, A. Baltuška, B. Shim, S.E. Schrauth, A. Gaeta, C. Hernández-García, L. Plaja, A. Becker, A. Jaron-Becker, M.M. Murnane, H.C. Kapteyn, Bright coherent ultrahigh harmonics in the keV X-ray regime from mid-infrared femtosecond lasers, *Science* 336 (2012) 1287, <http://dx.doi.org/10.1126/science.1218497>.
- [4] N. Thiré, R. Maksimenka, B. Kiss, C. Ferchaud, P. Bizouard, E. Cormier, K. Osvay, N. Forget, 4-W, 100-kHz, few-cycle mid-infrared source with sub-100-mrad carrier-envelope phase noise, *Opt. Express* 25 (2017) 1505–1514, <http://dx.doi.org/10.1364/OE.25.001505>.
- [5] N. Thiré, R. Maksimenka, B. Kiss, C. Ferchaud, G. Gitzinger, T. Pinoteau, H. Jousset, S. Jarosch, P. Bizouard, V. Di Pietro, E. Cormier, K. Osvay, N. Forget, Highly stable, 15 W, few-cycle, 65 mrad CEP-noise mid-IR OPCPA for statistical physics, *Opt. Express* 26 (2018) 26907–26915, <http://dx.doi.org/10.1364/OE.26.026907>.
- [6] B.W. Mayer, C.R. Phillips, L. Gallmann, U. Keller, Mid-infrared pulse generation via achromatic quasi-phase-matched OPCPA, *Opt. Express* 22 (2014) 20798–20808, <http://dx.doi.org/10.1364/OE.22.020798>.
- [7] M. Baudisch, H. Pires, H. Ishizuki, T. Taira, M. Hemmer, J. Biegert, Sub-4-optical-cycle, 340 MW peak power, high stability mid-IR source at 160 kHz, *J. Opt.* 17 (2015) 094002, <http://dx.doi.org/10.1088/2040-8978/17/9/094002>.
- [8] U. Elu, M. Baudisch, H. Pires, F. Tani, M.H. Frosz, F. Köttig, A. Ermolov, P. St.J. Russell, J. Biegert, High average power and single-cycle pulses from a mid-IR optical parametric chirped pulse amplifier, *Optica* 4 (2017) 1024–1029, <http://dx.doi.org/10.1364/OPTICA.4.001024>.
- [9] G. Fan, T. Balčiūnas, T. Kanai, T. Flöry, G. Andriukaitis, B.E. Schmidt, F. Légaré, A. Baltuška, Hollow-core-waveguide compression of multi-millijoule CEP-stable 3.2 μm pulses, *Optica* 3 (2016) 1308–1311, <http://dx.doi.org/10.1364/OPTICA.3.001308>.
- [10] P. Wang, Y. Li, W. Li, H. Su, B. Shao, S. Li, C. Wang, D. Wang, R. Zhao, Y. Peng, Y. Leng, R. Li, Z. Xu, 2.6 mJ/100 Hz CEP-stable near-single-cycle 4 μm laser based on OPCPA and hollow-core fiber compression, *Opt. Lett.* 43 (2018) 2197–2200, <http://dx.doi.org/10.1364/OL.43.002197>.
- [11] K. Murari, G.J. Stein, H. Cankaya, B. Debord, F. G  r  me, G. Cirmi, O.D. M  cke, P. Li, A. Ruehl, I. Hartl, K.-H. Hong, F. Benabid, F.X. K  rtner, Kagome-fiber-based pulse compression of mid-infrared picosecond pulses from a Ho:YLF amplifier, *Optica* 3 (2016) 816–822, <http://dx.doi.org/10.1364/OPTICA.3.000816>.
- [12] J. Schulte, T. Sartorius, J. Weitenberg, A. Vernaleken, P. Russbuehler, Nonlinear pulse compression in a multi-pass cell, *Opt. Lett.* 41 (2016) 4511–4514, <http://dx.doi.org/10.1364/OL.41.004511>.
- [13] G. Jargot, N. Daher, L. Lavenue, X. Delen, N. Forget, M. Hanna, P. Georges, Self-compression in a multipass cell, *Opt. Lett.* 43 (2018) 5643–5646, <http://dx.doi.org/10.1364/OL.43.005643>.
- [14] M. Hanna, X. Del  n, L. Lavenue, F. Guichard, Y. Zaouter, F. Druon, P. Georges, Nonlinear temporal compression in multipass cells: theory, *J. Opt. Soc. Am. B* 34 (2017) 1340–1347, <http://dx.doi.org/10.1364/JOSAB.34.001340>.
- [15] M. Ueffing, S. Reiger, M. Kaumanns, V. Pervak, M. Trubetskov, T. Nubbemeyer, F. Krausz, Nonlinear pulse compression in a gas-filled multipass cell, *Opt. Lett.* 43 (2018) 2070–2073, <http://dx.doi.org/10.1364/OL.43.002070>.
- [16] M. Hemmer, M. Baudisch, A. Thai, A. Couaeron, J. Biegert, Self-compression to sub-3-cycle duration of mid-infrared optical pulses in dielectrics, *Opt. Express* 21 (2013) 28095–28102, <http://dx.doi.org/10.1364/OE.21.028095>.
- [17] V. Shumakova, P. Malevich, S. Ališauskas, A. Voronin, A.M. Zheltikov, D. Faccio, D. Kartashov, A. Baltuška, A. Pugzlys, Multi-millijoule few-cycle mid-infrared pulses through nonlinear self-compression in bulk, *Nat. Commun.* 7 (2016) 12877.
- [18] F. Lu, P. Xia, Y. Matsumoto, T. Kanai, N. Ishii, J. Itatani, Generation of sub-two-cycle CEP-stable optical pulses at 3.5 μm from a KTA-based optical parametric amplifier with multiple-plate compression, *Opt. Lett.* 43 (2018) 2720–2723, <http://dx.doi.org/10.1364/OL.43.002720>.
- [19] A. Marcinkevi  t  , N. Garejev, R. Šuminas, G. Tamošauskas, A. Dubietis, A compact, self-compression-based sub-3 optical cycle source in the 3–4 μm spectral range, *J. Opt.* 19 (2017) 105505, <http://dx.doi.org/10.1088/2040-8986/aa873>.
- [20] M. Sheik-Bahae, D.C. Hutchings, D.J. Hagan, E.W. Van Stryland, Dispersion of bound electron nonlinear refraction in solids, *IEEE J. Quantum Electron.* 27 (1991) 1296–1309, <http://dx.doi.org/10.1109/3.89946>.
- [21] ELI-ALPS Research Institute, <https://www.eli-alps.hu/>.
- [22] Zhang Lin, Agarwal Anuradha M., Kimerling Lionel C., Michel Jurgen, Nonlinear group IV photonics based on silicon and germanium: from near-infrared to mid-infrared, *Nanophotonics* 3 (2013) 247, <http://dx.doi.org/10.1515/nanoph-2013-0020>.
- [23] D. Milam, M.J. Weber, A.J. Glass, Nonlinear refractive index of fluoride crystals, *Appl. Phys. Lett.* 31 (1977) 822–825, <http://dx.doi.org/10.1063/1.89561>.
- [24] D.N. Christodoulides, I.C. Khoo, G.J. Salamo, G.I. Stegeman, E.W. Van Stryland, Nonlinear refraction and absorption: mechanisms and magnitudes, *Adv. Opt. Photon.* 2 (2010) 60–200, <http://dx.doi.org/10.1364/AOP.2.000060>.
- [25] F. Silva, D.R. Austin, A. Thai, M. Baudisch, M. Hemmer, D. Faccio, A. Couaeron, J. Biegert, Multi-octave supercontinuum generation from mid-infrared filamentation in a bulk crystal, *Nat. Commun.* 3 (2012) 807.
- [26] S.B. Park, K. Kim, W. Cho, S.I. Hwang, I. Ivanov, C.H. Nam, K.T. Kim, Direct sampling of a light wave in air, *Optica* 5 (2018) 402–408, <http://dx.doi.org/10.1364/OPTICA.5.000402>.
- [27] W. Cho, S.I. Hwang, C.H. Nam, M.R. Bionta, P. Lassonde, B.E. Schmidt, H. Ibrahim, F. L  gar  , K.T. Kim, Temporal characterization of femtosecond laser pulses using tunneling ionization in the UV, visible, and mid-IR ranges, *Sci. Rep.* 9 (2019) 16067, <http://dx.doi.org/10.1038/s41598-019-52237>.
- [28] F. L  cking, V. Crozatier, N. Forget, A. Assion, F. Krausz, Approaching the limits of carrier-envelope phase stability in a millijoule-class amplifier, *Opt. Lett.* 39 (2014) 3884–3887, <http://dx.doi.org/10.1364/OL.39.003884>.
- [29] A. Marcinkevi  t  , V. Jukna, R. Šuminas, N. Garejev, G. Tamošauskas, A. Dubietis, Femtosecond filamentation and supercontinuum generation in bulk silicon, *Opt. Lett.* 44 (2019) 1343–1346, <http://dx.doi.org/10.1364/OL.44.001343>.
- [30] R.K.W. Lau, M.R.E. Lamont, Y. Okawachi, A.L. Gaeta, Effects of multiphoton absorption on parametric comb generation in silicon microresonators, *Opt. Lett.* 40 (2015) 2778–2781, <http://dx.doi.org/10.1364/OL.40.002778>.
- [31] W. Koechner, *Solid-State Laser Engineering*, Springer Science + Business Media, Inc., 2006.
- [32] R. Hollinger, D. Hoff, P. Wustelt, S. Skruszewicz, Y. Zhang, H. Kang, D. W  rzler, T. Jungnickel, M. Dumergue, A. Nayak, R. Flender, L. Haizer, M. Kurucz, B. Kiss, S. K  hn, E. Cormier, C. Spielmann, G.G. Paulus, P. Tzallas, M. K  bel, Carrier-envelope-phase measurement of few-cycle mid-infrared laser pulses using high harmonic generation in ZnO, *Opt. Express* 28 (2020) 7314–7322, <http://dx.doi.org/10.1364/OE.383484>.